ADVANCED ELECTRONIC MATERIALS Open Access
www.advelectronicmat.de

Understanding the Interplay Between Thermal Activation, Diffusion, and Phase Segregation of Molecular Dopants Blended with Polymeric Semiconductors

Francesca Pallini, Sara Mattiello, Mauro Sassi, Gabriele Paoli, Giuseppe Mattioli, Pietro Rossi, Giulia Coco, Alberto D. Scaccabarozzi, Brian Minki Kim, Pietro Mariani, Hiba Wakidi, Sadie M. Flagg, Massimiliano D'Arienzo, Mario Caironi, Thuc-Quyen Nguyen, and Luca Beverina**

Molecular doping of polymeric semiconductors is a key strategy to tune charge transport properties, energy levels alignment and charge injection in printed electronic devices. N-type doping is more challenging than p-type due to the characteristic energy levels of performing polymers requiring the development of oxygen sensitive dopants. Precursor dopants are kinetically stable compounds that cannot directly dope the target semiconductor but can be converted in situ via thermal activation into the real doping species. 1,3-Dimethyl-2-(4-(dimethylamino)phenyl)-2,4-dihydro-1H-benzoimidazole (N-DMBI-H) is the most widely employed example. While in blend with the polymeric semiconductor, the thermal activation of DMBI-H like molecules does not exclusively lead to doping but also causes diffusion and phase segregation of both the dopant itself and the various possible by-products of the doping cascade. All such processes have profound impact on the morphology, microstructure and charge transport properties of the blend. In this paper, we compare different DMBI-H derivatives with comparable thermodynamic doping capability over the benchmark polymer poly{[*N*,*N*′-bis(2-octyldodecyl)-naphthalene-1,4,5,8-bis(dicarboximide)-2,6-diyl]-alt-5,5′-(2,2′-bithiophene)} (P(NDI2OD-T2)) and we show how the phase segregation process is the main responsible for their different performances and dopant design can help enhance intermolecular interactions and reduce phase segregation.

1. Introduction

Solution processable organic semiconductors are key enabling materials for the development of a vast array of printable, mechanically flexible devices such as Organic Light-Emitting Diodes (OLEDs), Organic Field-Effect Transistors (OFETs), Organic Photovoltaics (OPV), Organic Photodetectors (OPDs), and Organic Thermoelectric Generators (OTEGs).[1–4] Alongside with solution processability conveying a dramatic reduction of production costs over established inorganic semiconductors, such materials hold promises of improved sustainability through the development of alternative raw materials, reduction of wastes associated with production and processing as well as enhanced biocompatibility fostering pioneering applications in biosensing, bioelectronics and even edible electronics.[5–9] When compared to their established inorganic counterparts, the intrinsically lower

F. Pallini, B. M. Kim, H. Wakidi, S. M. Flagg, T.-Q. Nguyen
Center for Polymers and Organic Solids
University of California at Santa Barbara
Santa Barbara, CA 93117, USA
E-mail: quyen@chem.ucsb.edu

S. M. Flagg
School of Materials Science and Engineering
Georgia Institute of Technology
Atlanta, GA 30332, USA

The ORCID identification number(s) for the author(s) of this article can be found under https://doi.org/10.1002/aelm.202500170

DOI: 10.1002/aelm.202500170

F. Pallini, S. Mattiello, M. Sassi, G. Paoli, P. Mariani, M. D'Arienzo, L. Beverina
Department of Materials Science
State University of Milano-Bicocca
Via Cozzi 55, Milano I-20126, Italy
E-mail: luca.beverina@unimib.it

G. Mattioli
Istituto di Struttura della Materia del Consiglio Nazionale delle Ricerche CNR-ISM
Via Salaria km 29.300, Monterotondo, RM 00015, Italy

P. Rossi, G. Coco, A. D. Scaccabarozzi, M. Caironi
Center for Nano Science and Technology
Istituto Italiano di Tecnologia
Via Rubattino, 81, Milano 20131, Italy

G. Coco, A. D. Scaccabarozzi
Department of Physics
Politecnico di Milano
Piazza Leonardo da Vinci 32, Milan 20133, Italy

charge transport properties of most organic semiconductors are responsible for the comparatively poorer figures of merits observed in nearly all organic (opto)electronic devices. The exception is OLEDs, where these limitations are counterbalanced by unique characteristic features such as thermally activated delayed fluorescence.[10] Just like in inorganic semiconductors, doping has a major influence in enhancing charge carrier density and thus conductivity over orders of magnitude. However, the fundamental nature of the doping process in organic materials differs from that of crystalline inorganic semiconductors. Materials can be p- or n-doped through direct electron transfer (ET) processes corresponding to oxidation (for p-type) and reduction (for n-type) reactions.[11,12] While in principle every material could be both p- and n-doped, semiconductors having relatively low lying LUMO (lowest unoccupied molecular orbital) levels are easier to reversibly reduce, thus preferentially undergoing n-type doping, whereas semiconductors featuring a high HOMO (highest occupied molecular orbital) level are more suitable for p-type doping.[13] So far, p-type doping proved to be far easier to control, as demonstrated by the performances achieved by commercially available materials such as PEDOT:PSS, offering conductivities above 1000 Scm^{-1} alongside with water processability,[11,12,14,15] and by other non-commercially available but easily accessible PEDOT based materials capable of exceeding conductivities of 6000 S cm^{-1}.[16,17] With the notable exception of some recently reported benzofuranedione-based polymers,[18,19] achieving similar performances with n-doped materials is significantly more challenging due to the relatively high energies of the LUMO levels of the materials – requiring the use of particularly strong reducing agents – and the consequent poor oxygen and moisture stability of the charge carriers created by the doping process.[20,21] Indeed, most high electron affinity (EA) organic semiconductors feature LUMO levels in the -4.0 to -3.8 eV energy region. Dopants such as tetrakis(dimethylamino)ethylene can perform a direct ET reduction at such energies but cannot be processed in air, requiring instead vacuum deposition techniques. The literature describes a valuable alternative approach consisting in the development of dopants that are unable to perform a direct ET reduction but that, once blended with the target semiconductor, can be converted into a much more reducing species by thermally or photochemically activated bond cleavage reactions.[22–26] Such precursor dopants possess a sufficient kinetic stability to enable processing under air as well as long term storage under inert conditions. 1,3-Dimethyl-2-(4-(dimethylamino)phenyl)-2,4-dihydro-1*H*-benzoimidazole (N-DMBI-H) is the most representative precursor-dopant of this kind, with documented capability of doping a wide variety of polymeric and molecular semiconductors including poly{[*N*,*N*′-bis(2-octyldodecyl)-naphthalene-1,4,5,8-bis(dicarboximide)-2,6-diyl]-alt-5,5′-(2,2′-bithiophene)} (P(NDI2OD-T2)), prototypical polymer for n-type purposes, and $PC_{60}BM$.[26–29] The details of the doping mechanism, a multi-step process culminating in an ET but also involving multiple bond cleavage and formation, are substrate dependent and still debated.[27,30–33] Although thermal activation is not always necessary for the activation of the dopant,[34] achieving high doping levels in solid blends require substantial annealing, also promoting diffusion and phase segregation. Careful optimization of processing conditions is key for best performances.[35]

Despite the commercial availability and hence, popularity of N-DMBI-H (**Scheme 1**), dopant:hosting polymer systems are far from being fully optimized. The primary limitation lies in the poor solid-state miscibility between the two components.[36] Indeed, the significant phase segregation generally observed upon thermal treatment results in doping being effective mainly at the interphase. Consequently, achieving high conductivity necessitates the use of dopant/polymer molar ratios exceeding 50 mol% (with respect to the repeating unit).[37] At such compositions, referring to such materials as "doped polymers" can be somewhat misleading, as the dopant:semiconductor system essentially forms a blend with specific properties that vary depending on the composition. Not only the pristine dopant shows massive bulk phase segregation, as well as blooming due to vertical segregation, but some of the products of the dopant parasite reactions with ambient oxygen can further impact on phase segregation acting as efficient nucleation seeds.[38] The development of alternative dopants focuses on reducing their tendency to phase segregate from the polymer via functionalization with aliphatic chains or on the introduction of electron donating groups, aiming at improving the driving force for the doping process.[28,32,36,39–41] Scheme 1 shows examples of dopants pertaining to the DMBI family.

Albeit successful in tuning the doping level and in some cases in preventing extensive vertical segregation at the surface, both approaches failed in providing the massive improvement in performances necessary to bridge the gap with p-doped polymers.

Recently, some of us proposed a different approach aimed at improving the dopant to polymer mutual miscibility via the engineering of specific interactions rather than on the general increase in degrees of freedom imparted by solubilizing chains. The IStBI dopant (**Scheme 2**) features an electron rich, antiaromatic dibenzoazepine moiety capable of providing stabilizing interactions with the electron-poor backbone of the target polymer P(NDI2OD-T2). The consequent reduction of the average dopant to polymer distance and of the competition with phase segregation afforded after suitable thermal annealing a maximum conductivity of 1.14×10^{-2} S cm^{-1}, the record value for P(NDI2OD-T2) based blends.[37]

Thermal annealing is necessary to activate the doping cascade, but at the same time it also favors diffusion of the precursor dopant.[42] On one side, diffusion is beneficial to enable efficient reaction between polymer and dopant but on the other it also triggers vertical phase segregation leading to blooming and bulk phase segregation through nucleation, particularly after the formation of nucleation seeds, as the doping proceeds.[35,38] The design of improved dopants is thus a complex and challenging task requiring control of the chemistry of the doping process as well as of the interplay between thermally activated diffusion, crystallization and vertical phase segregation. In this paper we devise guidelines for the design of improved dopants by comparing the morphological, structural and electrical properties of blends of the model n-dopable polymer P(NDI2OD-T2) with 6 different dopants offering diverse functionalization motifs, one of them being the prototypical N-DMBI-H. Scheme 2 shows that the analyzed dopants pertain to three different classes. IStBI and the new dopants PThBI and CBzBI feature a polycyclic, π-excessive heteroaromatic residue replacing the dimethylamine fragment of parent N-DMBI-H and can be considered dopants with extended

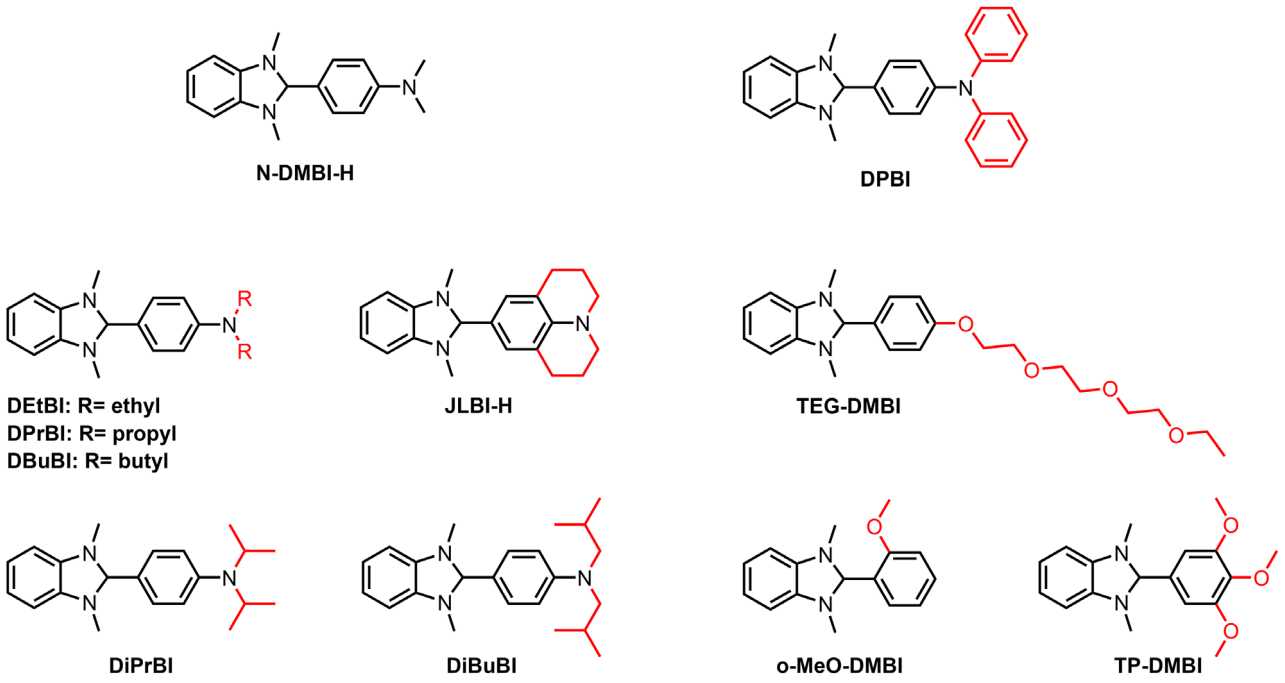

Scheme 1. Examples of DMBI derivatives. Structural variations with respect to the parent N-DMBI-H dopant are highlighted in red.

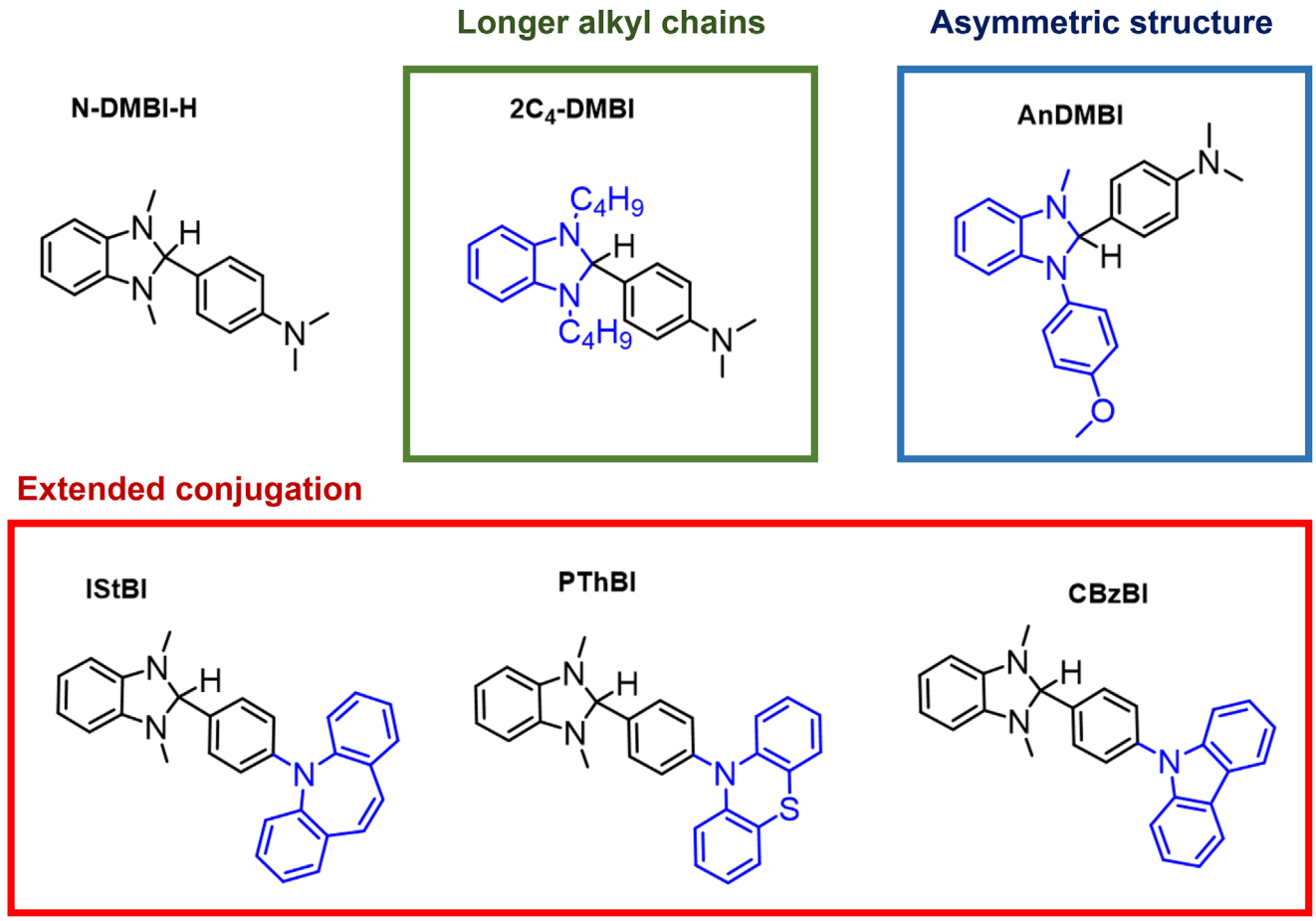

Scheme 2. Newly designed n-type molecular dopants.

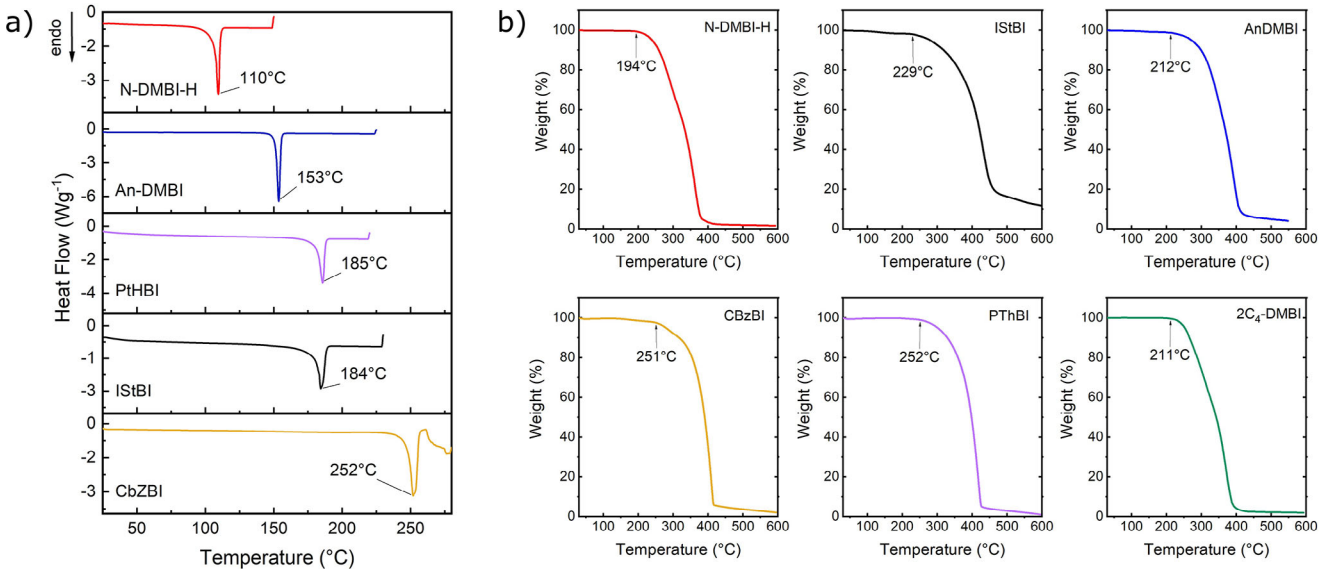

Figure 1. DSC a) and TGA b) traces of N-DMBI-H, $2C_4$-DMBI, AnDMBI, CBzBI, PThBI and IStBI. All traces recorded under N_2 stream. The DSC trace of $2C_4$-DMBI was not recorded as the material is a liquid at room temperature. The labelled value in (a) represents the melting temperature, while in (b) it indicates the on-set of thermal degradation. The whole thermal characterization is reported from a previous work from our group.[43]

conjugation. The original derivative $2C_4$-DMBI features two butyl chains aimed at improving solubility without altering the characteristic frontier orbitals energies. AnDMBI is the first example of the DMBI-H family featuring an aromatic substituent on the benzimidazole core instead of the widespread employed alkyl substituents.

Our results show that, thanks to the presence of the π-extended heteroaromatic structure, IStBI, PThBI and CBzBI all have an increased affinity for the polymer with respect to N-DMBI-H, resulting in comparatively less pronounced tendency to phase segregate. In the case of IStBI and PThBI this translates in higher doping efficiencies and conductivities. Conversely, $2C_4$-DMBI and AnDMBI show a phase segregation tendency even more pronounced than that of parent N-DMBI-H, thus leading to poorer performances. Although so far demonstrated only on P(NDI2OD-T2), our results show that obtaining efficient doping requires achieving control over all thermally activated phenomena influencing blend composition and morphology. The engineering of specific, noncovalent polymer/precursor dopant interactions is a valuable tool to prevent segregation, thus leading to good performances even at moderate doping levels. Computational tools can then dramatically help in understanding trends, allowing to correlate the dopants molecular structure and their diffusion tendencies in the semiconductor matrix, which is particularly challenging at the experimental level.

2. Results and Discussion

2.1. Characterization of the Dopants

We characterized all derivatives by means of thermogravimetric analysis (TGA) and differential scanning calorimetry (DSC) to assess thermal stability and to gain insight on their physical state when reaching the processing temperature, set at 180 °C for consistency with our previous studies on P(NDI2OD-T2)/IStBI blends.[37]

The comparison between the DSC (**Figure 1a**) and TGA (Figure 1b) traces shows that all new n-dopants are thermally stable at the annealing temperature of 180 °C and that, with the exclusion of CBzBI, at such temperature they are all above or very close to the corresponding melting point, thus favoring diffusion within the blend. CBzBI high melting point value is accompanied by a solubility in toluene below 2.0 g L^{-1}, far lower with respect to that of the other dopants, showing instead solubilities above 10 g L^{-1}.[43]

According to our previous investigation of the N-DMBI-H/P(NDI2OD-T2) blend, as well as other similar studies, doping can happen via homolytic cleavage of the C-H bond of the imidazoline pentatomic ring with formation of the N-DMBI• neutral radical species, eventually leading to doping via direct ET.[31,33] A recent computational work by Wang et al. further suggests that the driving force for the electron transfer reaction is highly determined by the ionization potentials of DMBI-H derivatives corresponding radicals, even in the case of a doping mechanism mediated by hydride transfer.[44] As such, the energy of the corresponding SOMO (Singly Occupied Molecular Orbital) level of the activated derivatives of the dopants reported in Scheme 2 is a significant gauge of the relative energetic landscape of the various doping processes. The position of the SOMO can be estimated experimentally via electrochemical measurement of the reduction potential of the corresponding oxidized benzimidazolium salts and calculated with good accuracy using DFT (Density Functional Theory). **Table 1** shows a comparison between experimental and calculated values for all derivatives as well as solubilities in toluene.

Calculated energies are in good agreement with the experimental ones. The electrochemical HOMO of N-DMBI-H has a −4.6 eV energy, while the SOMO of the corresponding neutral radical is located at −2.5 eV.[37] Both values agree with previous

Table 1. Solubilities and calculated (DFT) and experimental (Cyclic Voltammetry - CV - and Differential Pulse Voltammetry - DPV) HOMO and SOMO energy levels of the analyzed DMBI-H derivatives. Potentials obtained from CV measurements are also reported versus Ferrocene/ferrocenium redox couple. The results of the electrochemical characterization and the solubilities values are reproduced from ref. [43].

Dopant	E_{ox} [V] ($DH^{\bullet+}$/DH)	HOMO [eV]			E_{red}[V] (D^{+}/$D^{\bullet}$)	SOMO [eV]			Solubility [g L^{-1}]
		CV	DPV	DFT[a)]		CV	DPV	DFT[a)]	
N-DMBI-H	−0.19	−4.6	−4.6	−4.78	−2.26	−2.5	−2.5	−2.54	>100
IStBI	−0.19	−4.6	−4.6	−4.78	−2.17	−2.6	−2.6	−2.64	∼15
PThBI	−0.12	−4.7	−4.7	−4.90	−1.98	−2.8	−2.8	−2.97	∼15
CBzBI	−0.11	−4.7	−4.7	−4.89	−1.90	−2.9	−2.8	−2.95	∼1.7
AnDMBI	−0.09	−4.7	−4.7	−4.79	−2.13	−2.7	−2.7	−2.63	∼28
$2C_4$-DMBI	−0.22	−4.6	−4.6	−4.77	−2.19	−2.6	−2.6	−2.48	-

[a)] DFT values obtained using a composite method, illustrated in detail in the "Computational Methods" section.

reports using the same technique.[30,45] As expected, the energy levels of $2C_4$-DMBI are essentially identical to those of parent N-DMBI-H (−4.6 eV and −2.6 eV for HOMO and SOMO) according to the negligible change in the donating capabilities of butyl groups over methyl ones in the imidazoline nitrogen sites. The presence of the anisidyl residue in AnDMBI sizeably shifts the position of both HOMO and SOMO towards more negative values, showing that the delocalization of the imidazoline nitrogen lone pair over the benzene ring dominates over the electron donating effect of the methoxy substituent.

A similar effect is responsible for the stabilization of both HOMO and LUMO levels of all dopants featuring heteroaromatic donors with a more pronounced shift toward negative values for PThBI and CBzBI. As for the HOMO position, Fabiano et al. already discussed how in DMBI-like derivatives such level is mostly localized on the benzimidazoline ring and is thus negligibly responding to the substitution pattern of the phenyl portion.[45] The much more pronounced stabilization of the SOMO reflects the preferential delocalization of π-charge over the heteroaromatic ring with respect to the benzene one, also according to the non-negligible torsion angle between the two. The relatively higher SOMO of IStBI within the series is coherent with the antiaromatic character of dibenzoazepine.[46]

In summary, none of the "dopants" introduced can dope P(NDI2OD-T2) via direct ET but they all possess sufficiently high lying SOMO levels to be able to efficiently do so after thermal activation, as we also highlighted via EPR (Electron Paramagnetic Resonance) characterization (see Section S2, Supporting Information). As observed in our previous work,[37] no obvious difference in doping efficiency should thus be expected based on the exclusive evaluation of the energetic landscape of the dopants.

2.2. Computational Investigation of Diffusion Limited Phase Segregation of Dopant and Polymer

Even if EPR data (Figure S3, Supporting Information) suggest appreciable doping even at room temperature, literature agrees that achieving higher doping levels (and conductivity) requires thermal annealing at temperatures going from 100 to 150 °C and for periods going from 1 to 2 h, depending on the different protocols.[28,35–37] This suggests that doping is a comparatively slow process, competitive on such a time scale with nucleation/segregation. In the past we demonstrated how the introduction of nucleating agents can improve doping efficiency by reducing the average size of crystalline domains and thus increasing the interphase area.[38] An alternative scenario would require slowing down diffusion so that doping could significantly happen before phase segregation. On first approximation, diffusion depends on molecular weight but variations of this parameter along the series of dopants we developed (as well as in most known DMBI derivatives) are very limited. Further increasing of the molecular weight of the dopant could have unwanted plasticizing effects, severely reducing mobility. We instead endowed IStBI, PThBI and CBzBI with functionalities, i.e., the π-excessive heteroaromatic rings, capable of interacting with the polymer backbone, possibly limiting diffusion to the point that thermally activated doping becomes dominant over phase segregation/nucleation.

The measurement of temperature dependent diffusion coefficients of unreacted dopants within the polymer/dopant blend is challenging as the competing processes of doping and phase segregation cannot be decoupled. We therefore opted for a theoretical approach to provide a coherent framework for molecular interactions, and developed an original computational methodology based on molecular dynamics.

Using molecular mechanics simulations based on the GFN force field (GFN-FF), we compared the evolution of several random distributions of dopants and NDI2OD-T2 dimers – representative of the P(NDI2OD-T2) polymer – in a 1:1 ratio thus mimicking a 50 mol% doping concentration. The use of a dimer corresponding to two repeating units terminated with a thiophene ring at both ends instead of the full polymer was dictated by the need of a tradeoff between significancy and computational cost. Moreover, dimers are compatible with the formation of reasonably large globular aggregates that can be studied using simple radial parameters.

We thus simulated the evolution in time of the distance between the center of mass of the whole aggregates and the radial average of the center of mass of the dimers and dopants. Panels (a–f) in **Figure 2** show the results we obtained averaging 4 independent, 3 ns long, simulations at 500K (227 °C) for N-DMBI-H, $2C_4$-DMBI, AnDMBI, PThBI, CBzBI and IStBI, using a 12:12 dimer:dopant ensemble. We also performed two simulations 4 ns

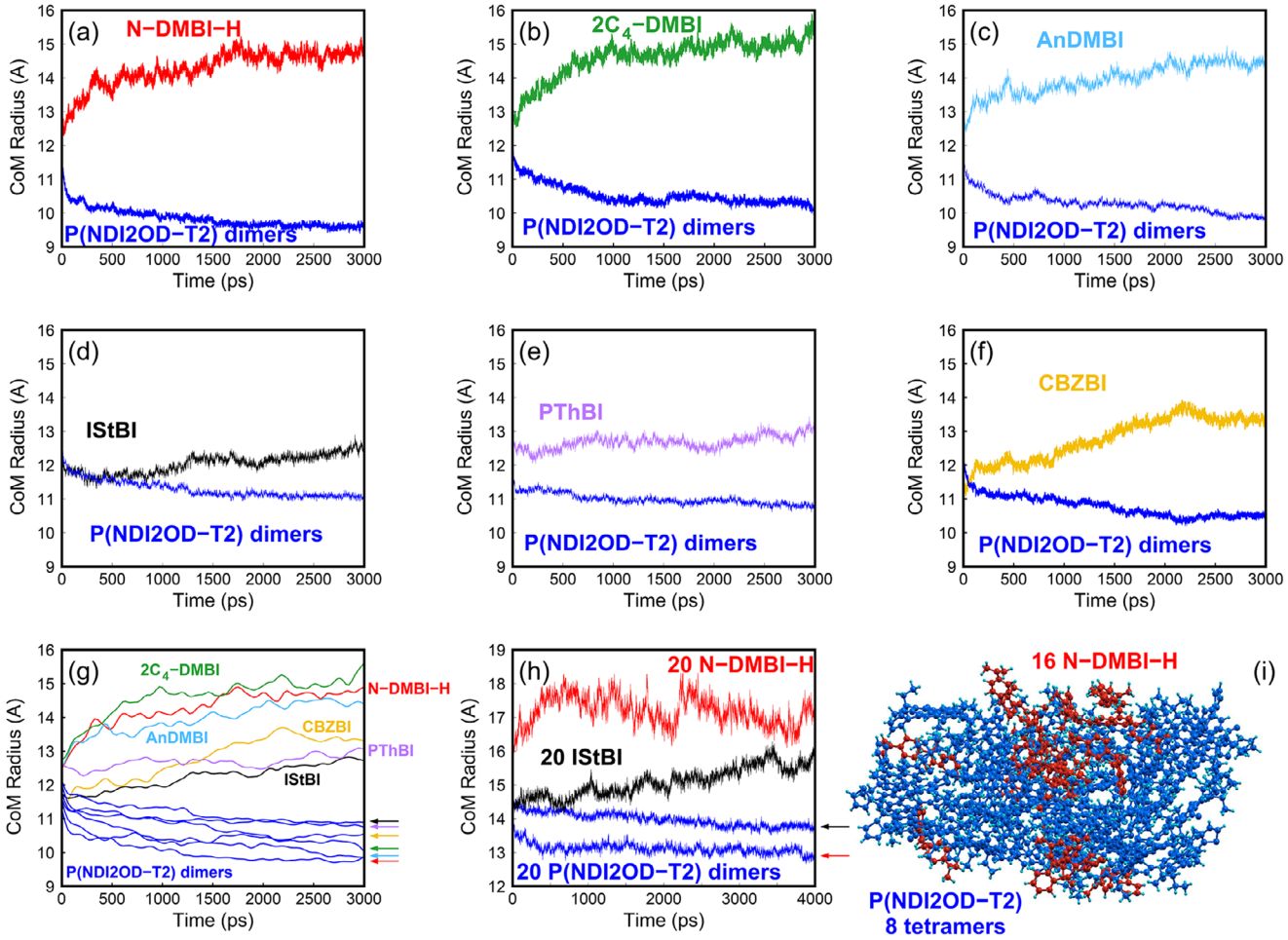

Figure 2. Time evolution of the distance between the center of mass of the whole aggregate and the radial average of the center of mass of the dimers and dopants for random ensembles of 12 NDI2OD-T2 dimers and 12 molecules of a) N-DMBI-H, b) $2C_4$-DMBI, c) AnDMBI, d) IStBI, e) PThBI, f) CBzBI dopants, along molecular dynamics (MD) trajectories @500K (227 °C). The splines of all plots (a-f) are shown together in panel g). Two plots related to larger systems of 20 dimers and 20 molecules are shown in panel h). A snapshot of the MD trajectory of an even larger system of 16 N-DMBI-H molecules and 8 NDI2OD-T2 tetramers after 3 ns of MD @ 500K is shown in panel i).

long, at 500 K, using a larger ensemble of 20:20 dimers:dopant using only N-DMBI-H and IStBI derivatives as representatives of limit behavior (panel h).

In the case of N-DMBI-H, $2C_4$-DMBI and AnDMBI, dopants and polymer dimers are clearly moving away from each other, with the dimers remaining closer to the ensemble center of mass and the dopants moving away from it, as graphically evidenced in Figure 2. PThBI, CBzBI and IStBI ensembles show a distinct behavior as the evolution of the average distance between each component and the center of mass of the aggregate appears to be much slower. In a nutshell, N-DMBI-H, $2C_4$-DMBI and AnDMBI rapidly diffuse away from the polymer, whilst PThBI, CBzBI and IStBI tend to maintain the original random distribution for a longer timeframe. Similar results have been obtained using larger aggregates such as those summarized in Figure 2h.

Figure 2i shows the result of a further simulation on an ensemble of 8 tetramers and 16 N-DMBI-H molecules clearly highlighting how the tetramers (in blue) form an elongated nanostructure of parallel chains, decorated on the surface by N-DMBI-H molecules (in red). On a much larger scale, this tendency would trigger extensive phase segregation.

The details of the specific dopant/polymer interactions can be better understood by studying monomer/dopants and dopant/dopant aggregates using the CREST (Conformer-Rotamer Ensemble Sampling Tool) algorithm and the xTB-GFN2 tight-binding Hamiltonian as engine, and then fully optimizing the most stable selected structures at DFT level of theory. The use of the monomer instead of the dimer is in this case dictated by the computational cost of DFT simulations. From the standpoint of the energetics involved, the monomer/monomer interaction is always stronger than the monomer/dopant one and the dopant/dopant interaction is generally weakly repulsive. After the doping event, the oxidized dopant/reduced monomer interaction becomes comparable with the monomer/monomer interaction. Details on the calculated interaction energies are reported in Section S5.1 of the Supporting Information. Such scenario explains the tendency to vertical separation and blooming for all the dopants but does not agree with the slower diffusion

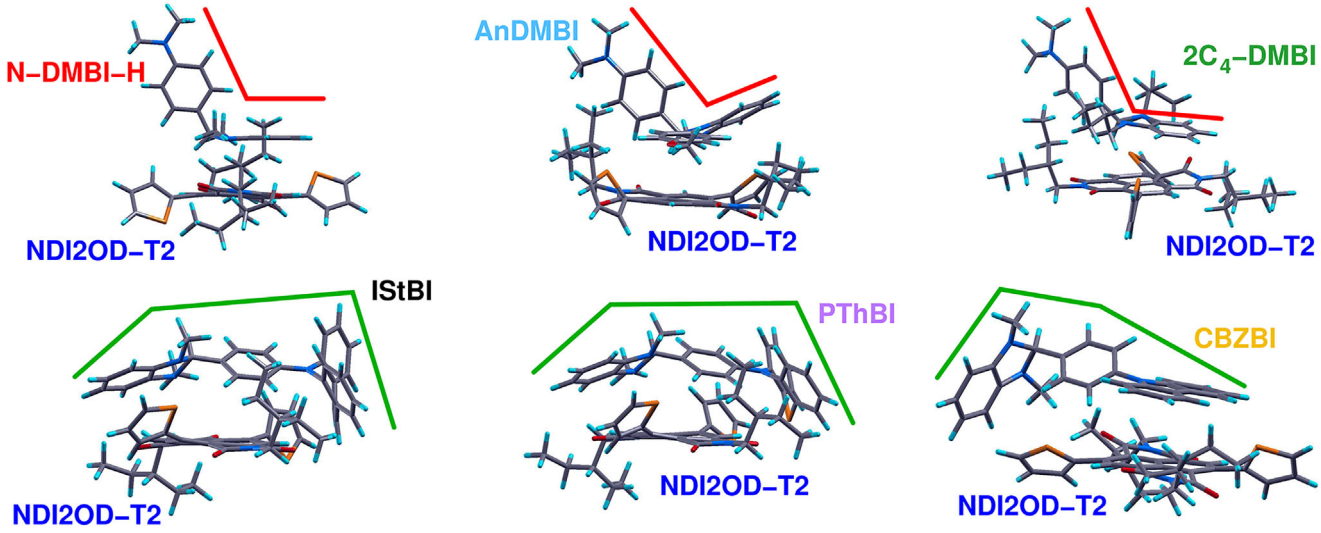

Figure 3. Ground state optimized geometrical structure (DFT) of monomer/dopant aggregates.

of IStBI, CBzBI and PThBI. Such phenomenon could be better rationalized by looking at the different conformations of the dopants we investigated. **Figure 3** shows the most stable structure of dopant/monomer aggregates for the different dopants. IStBI, CBzBI and PThBI have two joints that enable the molecules to wrap around the plane described by the naphthalene diimide (NDI) portion of the monomer, as suggested by green lines. Conversely, N-DMBI-H, $2C_4$-DMBI and AnDMBI have a single joint (red lines) preventing the same type of interaction and somehow keeping apart monomer molecules. The overall effect could be an opening up of the polymer structure, favoring diffusion and eventually vertical phase segregation. It should be mentioned that it was recently demonstrated that specific Dopant-Polymer interactions can also lead to improved doping capabilities induced by conformational changes, we did not explicitly investigate this interesting aspect.[34]

2.3. Optical Characterization of P(NDI2OD-T2)/Dopant Thin Films

The evolution of the optical features of thin films of P(NDI2OD-T2)/dopant blends at different dopant concentration provides a first characterization of the doping process. Undoped P(NDI2OD-T2) features a narrow, high energy absorption band with a maximum at 400 nm, assigned to the $\pi-\pi*$ transition, and a broader charge transfer band with a maximum at 705 nm, associated with the intrachain charge transfer (ICT) between the donor and acceptor units in the polymer chain. P(NDI2OD-T2) also features spectral signatures of aggregates in the low energy portion of the ICT band.[47] Addition of dopants leads to a progressive bleaching of the ICT band, alongside with the formation of a new band peaked at around 500 nm and an absorption tail above 800 nm. These two features belong to polymer polaron states, as previously assessed on the basis of spectroelectrochemistry and charge modulation spectroscopy evidences.[48,49] **Figure 4** shows the UV-Vis-NIR absorption spectra of thin films of the various polymer/dopant blends as the function of increasing dopant concentration, obtained by spin coating from toluene and thermally annealed at 180 °C for 2 h.

The trend observed with N-DMBI-H is in line with analogous studies already reported in the literature. The bleaching of the ICT band and the formation of the new polaron features are highlighted with blue and red arrows. Although the trend is clearly recognizable, the overall evolution of optical features is minimal, in agreement with the general observation that doping is inefficient with this derivative.[36] The behavior of the other dopants can be divided in two classes, corresponding to the very same ones we identified in the computational simulations of the diffusion processes. AnDMBI and $2C_4$-DMBI behave very similarly to N-DMBI-H. CBzBI shows a similar behavior to N-DMB-H as well. Conversely, doping with PThBI and IStBI leads to a much more pronounced bleaching of the ICT band, a clear and progressive strengthening of the polaron bands at 500 and 800 nm, as well as a progressive blueshift of the high energy transition at 400 nm due to contributions of the high energy absorption band of the radical states.[49] The data shows that extended conjugation dopants are generally more efficient in increasing the overall doping level, non-necessarily leading to better charge transport properties as this is also related to changes in the morphology impacting on the degree of crystallinity of P(NDI2OD-T2).[50]

2.4. Structural and Morphological Characterization of P(NDI2OD-T2)/Dopant Films

Grazing incidence wide angle X-ray scattering (GIWAXS) offers insights into the bulk microstructure of polymer:dopant blends. Regarding this point, an addition of N-DMBI-H to P(NDI2OD-T2) does not usually lead to disruptions of the microstructure of the latter; indeed GIWAXS patterns show the typical diffractions of the polymer– with crystals that are mainly face-on oriented. Other benzimidazoline-based dopants, including IStBI, have been reported to slightly affect the polymer crystal stacking distance because of an intercalation of dopant molecules within polymer chains.[28,37] Thus, here we assessed the impact of the

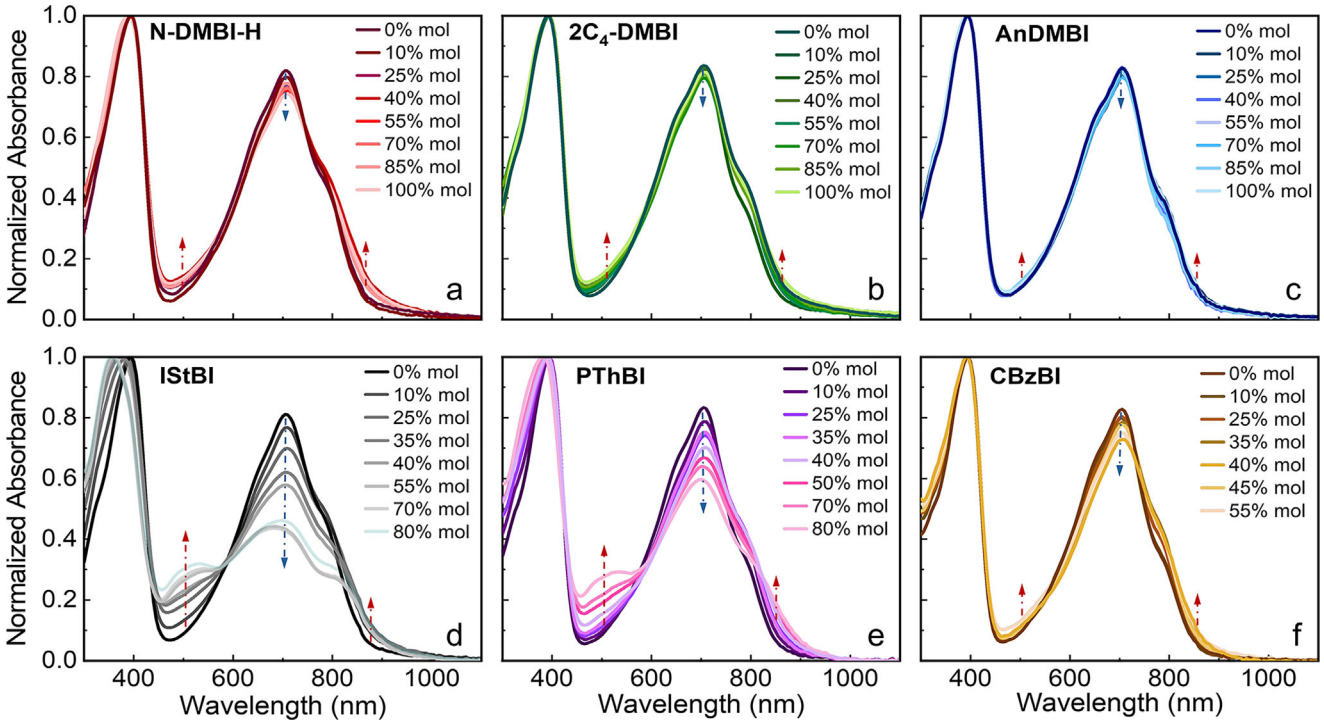

Figure 4. UV–Vis-NIR absorption spectra of P(NDI2OD-T2) films doped with different molar concentrations of N-DMBI-H a), $2C_4$-DMBI b), AnDMBI c), IStBI d), PThBI e) and CBzBI f). Spectra were normalized with respect to the π-π* transition peak ($\lambda \approx 394$ nm). The appearance of polaron related absorption features and the bleaching of the polymer charge transfer band are highlighted with red and blue arrows respectively.

whole dopants series under study on the solid-state microstructure of P(NDI2ODT2) thin films via GIWAXS. Films comprising 40 mol% of dopant with respect to the polymer repeating unit were annealed at the temperature of 180 °C for 2 h, according to our previous experience with IStBI/P(NDI2OD-T2) blends, which show the best electrical performances under similar conditions. **Figure 5** shows the 1D sector averaged diffractograms for the different blends, realized by performing linecuts of 2D-GIWAXS patterns along the in-plane (IP) and out-of-plane (OOP) directions. The complete 2D diffraction patterns are included in Figure S4 (Supporting Information).

All spectra show the diffraction features typical of P(NDI2OD-T2) crystalline domains arranged face-on with respect to the substrate, with a partial edge-on conformation. A majority face-on component is related to the marked IP (h00) and IP (00l) replicas and to the OOP (010) peak, which are assigned respectively to the lamellar, backbone, and π–π stacking. The OOP (h00) features are instead associated with the lamellar stacking of edge-on oriented regions.[51,52] Dopant related features are absent in most diffractograms. The only exception are N-DMBI-H doped films related measurements that, contrary to previous reports, show diffractions associated to the nucleated N-DMBI-H crystalline phase (see Figure S7, Supporting Information) hinting at a clear phase segregation between the polymer and the dopant.

The diffractions features related to the P(NDI2OD-T2) chain backbone repeat are not affected by the presence of the dopant, suggesting that order is preserved on the local scale. The impact on the in plane (h00) replicas is generally more sizeable and dopant dependent. AnDMBI and $2C_4$-DMBI behave in a more similar way to N-DMBI-H and have little or no impact on the diffractogram, conversely the presence of all the extended conjugation dopants shifts the (h00) vector values toward higher q, with the (100) peak moving from the reference q value of ≈2.47 nm^{-1} to $q \approx 2.60$ nm^{-1}. This feature, which we previously observed in films doped with IStBI, corresponds in real space to a shrinkage of the lamellar d spacing from a value of ≈2.54 nm to that of ≈2.42 nm. This feature could be attributed to intercalation of the dopant between the polymeric conjugated backbones, leading to conformational changes in its branched alkyl side chains.[28,37] This hypothesis is further supported by the reduction of the intensity of the (010) OOP π-π stacking peak – visible only in the diffraction patterns of blends containing extended conjugation dopants – and coherent with a perturbation of the average π-π interaction of polymer crystalline domains. The (010) peak intensity reduction is accompanied by a small shift of the q vector to lower values, as highlighted in Section S3.2 of the SI for IStBI doped films, which hints at an expansion of the crystal lattice along the π-π stacking direction, further supporting the intercalation hypothesis. This experimental evidence matches well with the presented DFT modelling results suggesting a higher tendency of this subset of derivatives to efficiently "wrap" around the polymer molecular structure. Thus, GIWAXS supports a stronger interaction inside the more ordered polymer domains with extended conjugation dopants with respect to parent N-DMBI-H, AnDMBI and $2C_4$-DMBI. For a subset of dopants, we analyzed as cast films and films annealed at a lower temperature of 80 °C (see Figures S5–S9, Supporting Information) as well, highlighting similar trends. Nonetheless,

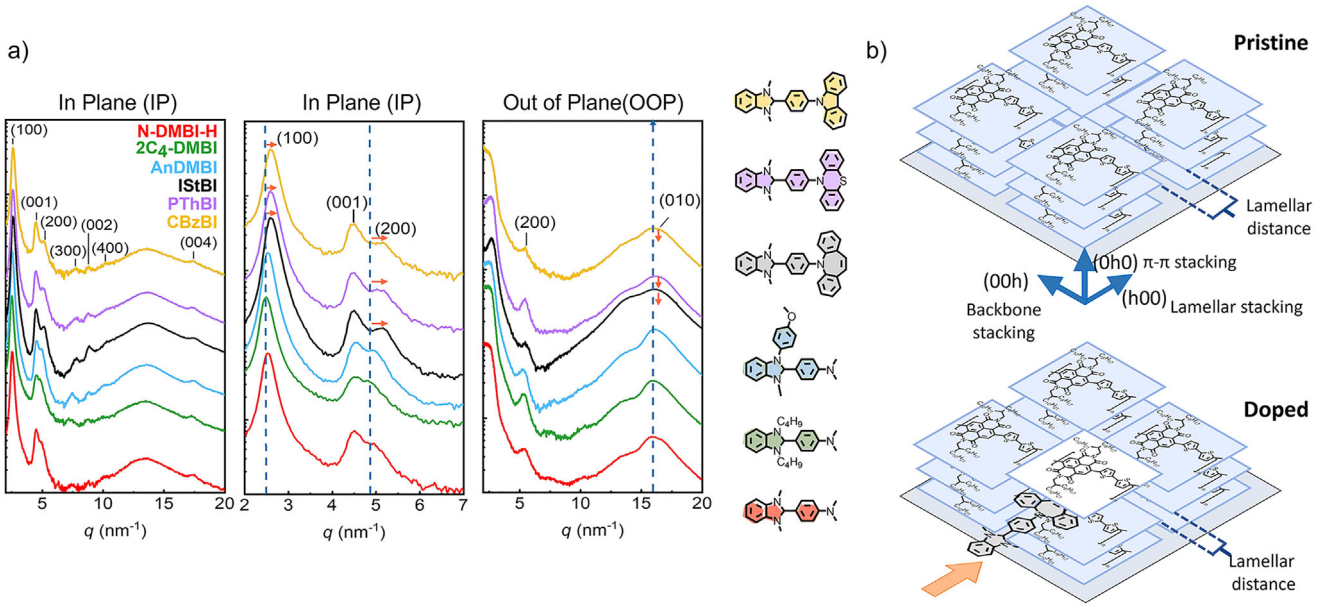

Figure 5. a) Sector averaged 1D profiles along the IP and along the OOP direction of the 2D GIWAXS patterns of P(NDI2OD-T2) films doped with 40% mol of N-DMBI-H (red), AnDMBI (blue), $2C_4$-DMBI (green), IStBI (black), PThBI (purple) and CBzBI (yellow). The IP profile is reported from 2 to 20 nm^{-1} q vector values as well as at a magnification between 2 and 7 nm^{-1}. Peaks associated with the most noticeable changes are highlighted with orange arrows and dashed blue lines. b) Cartoon representation of the effect of dopant slip stack between polymer chains resulting in widening of π-π stack interactions and reduction of lamellar distance.

we generally observed only minor changes in P(NDI2OD-T2) peak position in such samples with respect to samples treated at 180 °C, which suggests that microstructural reorganization and dopant/polymer interactions mainly happen during thermal treatment, together with dopant activation. Phase separation of this class of dopants typically affect the surface topography of P(NDI2OD-T2) films.[28,36] Therefore, to evaluate the possible impact of microstructural findings on phase separation, we performed an atomic force microscopy (AFM) analysis on films having the same composition as those analyzed via GIWAXS. We included a neat polymer film as reference. **Figure 6** shows the AFM images, along with the corresponding values of Root Mean Square (RMS) surface roughness. All the films show the typical elongated fibrillar structure topography of pristine P(NDI2OD-T2), when casted from toluene.[53] Once again, extended conjugated dopants and solubilized ones have a different behavior, with the former consistently showing smoother surfaces and finer fiber structures and the latter showing instead coarser surfaces similar to those observed for N-DMBI-H. Such differences in topographical features again point towards a different dopant-polymer interaction and dopant diffusivity, which well matches with the results of our GIWAXS characterization and computational studies. The formation of a rough surface is generally interpreted as hint for phase segregation, in some cases leading to the formation of clearly visible dopant domains at the surface.[28,36,39] In the case of a PThBI/polymer blend where surface segregates were evident, we performed a conductive AFM study giving further evidence on the insulating nature of such surface structures (Figure S11, Supporting Information).

Further increase of the dopant concentration to 70 mol% (55 mol% in the case of CBzBI due to this dopant poor solubility in toluene) leads to generally higher surface roughness but it does not change the overall picture that extended conjugation derivatives feature a less pronounced tendency to phase separation. AFM images at 70 mol% dopant concentration are shown in Figure S10 of the Supporting Information.

2.5. Electrical Characterization of the P(NDI2OD-T2)/Dopant Blends

Figure 7a shows the σ values as the function of the doping level for all dopants considered in the present study. We included N-DMBI-H as the reference as well as the previously reported IStBI to compare data acquired under comparable experimental conditions. We mixed polymer and dopants – in concentration between 10 and 100 mol% in toluene, deposited the films by spin coating and performed the standard thermal annealing treatment at 180 °C for 2 h prior to electrical characterization. In the case of CBzBI, the maximum dopant concentration we were able to reach was 55 mol% due to a limited solubility in toluene. The values we obtained for N-DMBI-H are in line with those previously reported in similar experiments, with a maximum conductivity value of around 1.3×10^{-3} S cm^{-1} at 70 mol%.[28,45,54]

The results show different trends for solubilized versus extended conjugation dopants. Doping with AnDMBI and $2C_4$-DMBI gives results comparable with those obtained with N-DMBI-H at low dopant concentrations (10 mol%). Above the 10 mol% threshold, the σ values stabilize at around 10^{-4} S cm^{-1} for $2C_4$-DMBI and oscillates between 10^{-4} and 5×10^{-5} S cm^{-1} for AnDMBI. For all extended conjugation derivatives, σ keeps increasing up to the 40 mol% doping concentration, eventually stabilizing or slightly reducing at higher concentrations. As already reported, IStBI top conductivity significantly outperforms

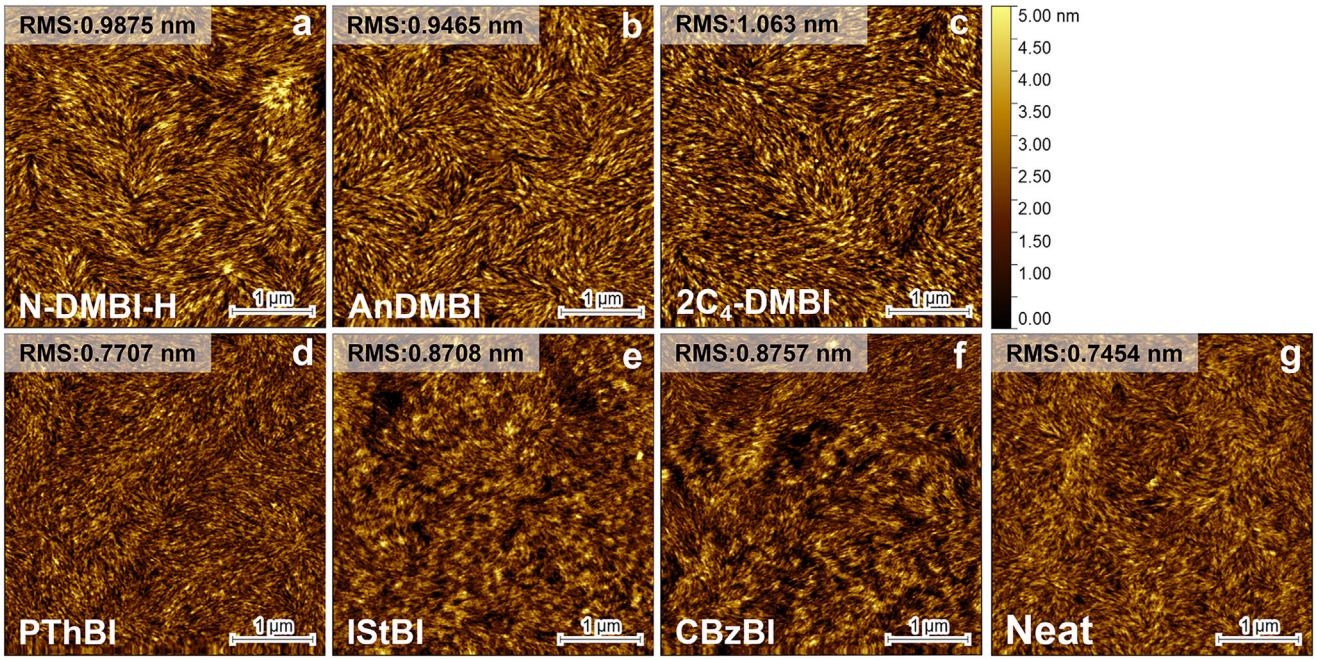

Figure 6. 4 µm × 4 µm AFM topography images (scale bar: 1 µm) of P(NDI2OD-T2) doped with of N-DMBI-H a), AnDMBI b), $2C_4$-DMBI c), PThBI d), IStBI e) and CBzBI f) at a concentration of 40 mol%, together with their Root Mean Square Roughness (RMS). An image of a neat P(NDI2OD-T2) annealed film is reported as well as comparison g).

N-DMBI-H, reaching a maximum value just above 10^{-2} S cm^{-1}. PThBI shows a similar trend, peaking at 0.2×10^{-2} S cm^{-1}. CBzBI behavior is essentially superimposable to that of N-DMBI-H. Figure 7b shows that the RMS and peak conductivity value at the same dopant concentration are correlated, with smoother samples showing higher conductivities.

Optimizing the conductivity of polymer/dopant blends is an intrinsically multivariate problem and drawing general conclusions based on the data we discussed could be misleading, yet our results are coherent with the following rationalizations. The behavior of the solubilized dopants $2C_4$-DMBI and AnDMBI is dominated by phase segregation issues. Even if energetically very similar to N-DMBI-H, they are both inefficient in doping (as assessed by the UV–vis data), do not sizably interact with the polymer (as shown by GIWAXS, as well as computational studies) and show higher tendency to phase separation (AFM). Conversely, based on the same set of evidence, conjugation extended dopants show improved doping capabilities, enhanced interactions with the polymer with consequent reduced tendency to phase segregate. Within this subclass, the behavior of CBzBI is affected by both a particularly poor solubility in toluene and a characteristically high melting point. Likewise, even if the computational analysis still suggests an improved interaction with the polymer with respect to N-DMBI-H, the driving force for phase

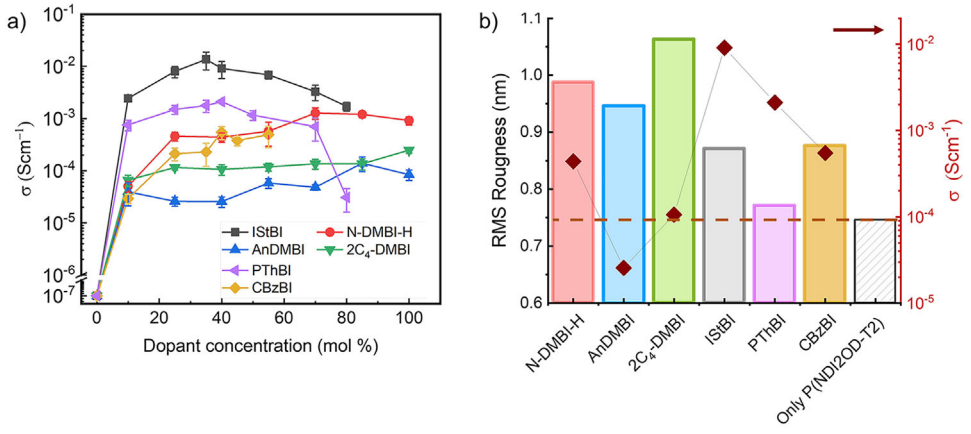

Figure 7. a) Conductivity σ of P(NDI2OD-T2) films doped with N-DMBI-H (red dots), $2C_4$-DMBI (green triangles), AnDMBI (blue triangles), IStBI (black squares), PThBI (purple triangles) and CBzBI (yellow diamonds) as the function of the dopant concentration. b) Comparison between the RMS roughness (histograms) and conductivity (red diamonds) for 40 mol% blends of dopants and P(NDI2OD-T2). Same color coding applies.

segregation remains dominant, leading to both poor doping efficiency and reduced conductivity. Both IStBI and PThBI outperform N-DMBI-H with the former offering best overall doping efficiency and conductivity, possibly due to more favorable SOMO energy.

3. Conclusion

N-type doping of organic semiconductors presents specific challenges with respect to p-doping, mostly due to the limited electron affinity of performing materials. Strongly reducing agents capable of direct electron transfer reactions can be used but require careful control of the environment to avoid degradation. Precursor dopants of the DMBI-H class are stable enough to enable processing under ambient conditions but are thermodynamically unable to directly dope the target semiconductor. Thermal annealing activates different reaction pathways, eventually leading to the in situ formation of suitable reducing agents. This process cannot be decoupled from similarly thermally triggered diffusion and phase segregation of the dopant from the polymeric host. Both processes have a detrimental effect on doping and thus conductivity and should be minimized to improve performances. We have shown how details in the chemical structure of the dopant may have a limited impact on the energy landscape of the doping cascade while still profoundly influencing doping efficiency and ultimately performances. Indeed, by combined computational, structural, optical, magnetic and electrical characterization we show that dopants possessing structural features capable of favorably interacting with the host polymer display a comparatively less pronounced tendency to diffuse and phase segregate. This enables more efficient doping and thus achieving of a higher charge carrier density at the same dopant concentration, ultimately leading to higher conductivities. Our findings have profound consequences on the development of alternative guidelines for next generation precursor dopants. While most of the existing literature emphasizes the need for solubilizing chains as a tool to limit phase segregation, our data show that the introduction of moieties favoring interaction with the host polymer is an additional relevant feature to be considered. This concept is showcased particularly by the iminostilbene functionalized IStBI dopant, featuring both suitable processability and limited tendency to phase segregation leading to the best doping performances ever reported in the literature with the benchmark polymer P(NDI2OD-T2).

4. Experimental Section

Preparation and Characterization of Films Doped with Different DMBI Derivatives: P(NDI2OD-T2)[55] polymer was synthesized via direct arylation reaction adapting a literature procedure reported by Sommer et al.[56] Two different batches were obtained and used in this work, having M*n* of 26.2 kDa (PDI: 2.65) and 37.3 kDa (PDI: 3.46) respectively (see Figure S1, Supporting Information for GPC characterization results). In the case of the first batch (M*n* of 26.2 kDa), commercial $Pd_2(dba)_3$ (Strem Chemicals) was used as catalyst. For the preparation of the second batch (M*n*: 37.3 kDa) $Pd_2(dba)_3$ catalyst was instead purified according to a procedure reported by Zalesskiy and Ananikov prior to its use.[57] The first batch was used for electrical conductivity measurements, AFM analysis and optical characterization of films doped with most of the derivatives and for all EPR measurements. Characterization of films doped with PThBI and CBzBI was instead performed using the second batch, as well as all GI-WAXS analyses. Molecular weights of the polymers were measured via Gel Permeation Chromatography at the Material Research Laboratories (MRL at UCSB). Measurements were performed using an Alliance HPLC System (2695 Separation Module, by Waters), equipped with a Tosoh TSKgel SuperHZM-N and a guard column (MW range: 200–700,000 g mol^{-1}), a Waters 2998 Photodiode Array Detector (PDA) and a Waters 2410 Differential Refractometer (RI) detector. Chloroform with 0.25% of triethylamine (TEA) was selected as solvent. Polystyrene was used as reference. Synthesis of DMBI derivatives was performed according to a procedure previously reported by this group.[43] It was known that N-DMBI-H derivatives can undergo degradation when exposed to air, especially if in solution, leading to the formation of a specific decomposition product impacting on doping performances.[30,37,38] Due to this air sensitivity issue, all the dopants were stored under inert atmosphere. It was noticed that oxidation issues were particularly relevant in the case of $2C_4$-DMBI. As such, procedures involving this derivative were performed with additional care to avoid any air exposure.[55]

Thin Films Preparation Procedure: The whole procedure was performed inside a glove box in an N_2 atmosphere (O_2 < 5 ppm). A P(NDI2OD-T2) polymer solution was prepared at a concentration of 12 g L^{-1} using anhydrous toluene. The mixture was stirred at 60 °C for at least 12 hours to ensure complete polymer dissolution and was filtered through a 0.45 µm PTFE syringe filter prior to its use. Solutions of N-DMBI-H, $2C_4$-DMBI, AnDMBI, IStBI, PThBI and CBzBI were prepared under N_2 atmosphere, at room temperature at concentrations of 10 g L^{-1}, 13 g L^{-1}, 7 g L^{-1}, 5 g L^{-1}, 2.8 g L^{-1}, 1.7 g L^{-1} respectively, using anhydrous toluene as solvent. Aliquots of dopant and polymer solutions were mixed at room temperature to achieve the desired dopant concentration. Toluene was then added to each dopant and polymer mixture to reach the same P(NDI2OD-T2) concentration (between 5 g L^{-1} and 8.75 g L^{-1} depending on the dopant used). The resulting solutions were used within 1 hour from preparation.

Glass substrates were prepared by cutting microscope slides into 15 mm × 15 mm pieces. The substrates were cleaned with deionized water, acetone and 2-propanol (20 minutes treatment in ultrasonic bath per each solvent), and subsequently oven dried. For electrical conductivity measurements, the glass substrates were patterned with metallic contacts using a shadow mask and an Angstrom Engineering evaporator (5 nm Cr adhesion layer, followed by a 50 nm Au layer). Three active channels were obtained on each substrate, having dimensions (width × length) of 14 mm × 2.5 mm, 7 mm × 2.5 mm and 6 mm × 3 mm, respectively. The cleaning procedure was repeated, and the substrates were exposed to UV-Ozone treatment for 10 minutes. Polymer films were then spin-cast onto the substrates from solutions (1000 rpm for 60 seconds, 3000 rpm for 5 seconds) and annealed at 180 °C for two hours in an inert atmosphere. The obtained film thickness was evaluated either using an AMBIOS XP-100 profilometer or with AFM, yielding average thicknesses of 50 ± 8 nm for N-DMBI-H, 37 ± 6 nm for AnDMBI and $2C_4$-DMBI, 40 ± 7 nm for IStBI, 26 ± 3 nm for PThBI and 23 ± 6 nm for CBzBI. The film used for evaluation of the pristine polymer conductivity was prepared according to the same procedure, with a 11 g L^{-1} polymer solution (film thickness 70 ± 5 nm).[55]

Electrical Characterization: The I–V characteristics of the films were measured using a two-point contacts configuration with a Signatone 1160 Series Probe-Station connected to a Keithley 4200 Semiconductor Parameter Analyzer. Measurements were carried out at room temperature in a N_2-filled glovebox, performing forward and backward scans to exclude presence of hysteresis. The electrical conductivity (σ) was then calculated according to the formula $\sigma = l/(Rwt)^{-1}$, where t was the film thickness, l was the active channel length, w was the active channel width and R was the resistance values extrapolated from the I–V curves. Conductivity was evaluated as the average of the values measured from the three active channels present on each sample. Error bars were calculated considering the standard deviation on the average value and the uncertainty in the film thickness evaluation.[55]

Optical Characterization of Thin Films: Films for optical characterization were prepared using the same solutions and according to the same procedure as those obtained for electrical characterization, but using 2 cm × 2 cm glass substrates. UV-Vis-NIR absorption spectra of the films were

acquired in the 1200–3000 nm range with a Lambda 750 UV/Vis Spectrometer by Perkin Elmer. All the samples were kept inside an N_2 filled glove box and were exposed to air just a few seconds prior to spectrum measurement.[55]

AFM Characterization: Film for AFM measurements were prepared following the same procedure as those used for electrical characterization. Samples were stored under an inert atmosphere prior to characterization. AFM images were acquired using a Veeco-Bruker Multimode AFM operating in tapping mode, with an AFM tapping tip (BudgetSensors, Tap300-G) featuring a force constant of 40 Nm^{-1} and a resonant frequency of 300 kHz. Images were then analyzed using Gwyddion software.[55]

GIWAXS Measurements: Preparation of samples for GIWAXS measurements followed the same procedure used for electrical characterization but using p-type silicon substrates instead of glass. All samples were prepared using solutions characterized by a dopant concentration of 40% in moles with respect to the polymer repeating unit. Toluene aliquots were added to each solution to achieve the same polymer concentration, in order to obtain films with similar thickness. The obtained films were then sealed under vacuum and analyzed within 30 minutes from air exposure.

GIWAXS performed at the BL11, NCD-SWEET, beamline at ALBA Synchrotron, Cerdanyola del Vallès (Spain). The energy beam was set to 12.4 keV (λ = 0.1 nm), with a channel-cut Si (1 1 1) monochromator and a Rayonix LX255-HS area detector (pixel size: 88 microns). The sample to detector distance was 201.346 mm, with exposition time of 5 s. 2D-GIWAXS patterns were corrected as a function of the components of the scattering vector using a MATLAB script developed by Aurora Nogales and Edgar Gutiérrez.[58]

Computational Methods: Atomistic simulations of P(NDI2OD-T2)/dopant systems have been carried out using a multi-level protocol.[55] Regarding pristine and activated dopants, the most stable conformers of the molecules have been individuated using a conformer-rotamer ensemble sampling tool (CREST),[59] based on the GFN2-xTB tight-binding Hamiltonian as "engine" for the calculations of energies and forces.[59,60] Then, the electronic properties of the structures found by CREST have been investigated using density functional theory simulations, performed in a GTO framework by using the ORCA suite of programs.[61] In detail, the Kohn-Sham orbitals have been expanded on the all-electron def2-TZVPP Gaussian-type basis set.[62,63] The corresponding def2/J basis has been also used as an auxiliary basis set for Coulomb fitting in a resolution-of-identity/chain-of-spheres (RIJCOSX) framework. Molecular geometries have been fully optimized and their properties investigated by using the B3LYP functional,[64] with the addition of the pairwise D3 correction for the calculation of dispersion forces.[65] Moreover, redox potentials of all the molecules have been calculated using the M06-2X hybrid functional[66] and the def2-TZVPP basis set, reoptimizing all geometries starting from B3LYP results. The molecules and their positive/negative ions have been embedded in an implicit CH_2Cl_2 solvent using a conductor-like polarizable continuum model (CPCM)[67] to calculate electronic and solvation energies. Thermochemical properties of the same molecules have been calculated using the B3LYP functional introduced above. Redox potentials have been then calculated as ΔG values between neutral and charged species. Finally, the very same framework has been used to calculate the properties of monomer/monomer, dopant/dopant and monomer/dopant dyads in several configurations, as reported in the SI. For the sake of clarity, to use T-NDI2OD-T was chosen as repeating unit of all the P(NDI2OD-T2) oligomers investigated. All molecular-mechanics simulations have been performed using the GFN force field.[68] Preliminary calculations have been performed using all the systems calculated at DFT level as a benchmark to verify that GFN-FF was able to provide the same qualitative description of noncovalent interactions of DFT (results in the SI). To investigate the evolution of P(NDI2OD-T2)/dopant blends upon thermal activation, structures were generated containing P(NDI2OD-T2) oligomers and dopants in a 2:1 ratio between NDI2OD-T2 monomers and molecules, randomly distributed using the Packmol tool[69] inside spheres having diameters variable between 4.5 and 6.5 nm. All the structures have been first fully optimized and then heated at 500 K using a Berendsen thermostat and evolved for 3–5 ns with a time step of 2 fs for the integration of the equation of motion. Most of the calculations have been performed using 12 NDI2OD-T2 dimers and 12 dopant molecules, because such aggregates tend to keep a globular shape and can therefore be studied using simple radial parameters and were big enough to have a clear differentiation between cluster surface and bulk. Key parameter of the present study was the average radial distance of the center of mass of oligomers and dopants from the center of mass of the whole aggregate. Four independent simulations for each dopant have been started by different random structures, and the results averaged. Further simulations have been performed using blends of 20 dimers and 20 dopants, and a single run has been carried out using 8 tetramers and 16 N-DMBI-H molecules.

Supporting Information

Supporting Information is available from the Wiley Online Library or from the author.

Acknowledgements

L.B., M.S., and S.M. gratefully acknowledge financial support from MUSA (Multilayered Urban Sustainability Action – project, funded by the – NextGenerationEU, under the National Recovery and Resilience Plan (NRRP) Mission 4 Component 2 Investment Line 1.5: strengthening of research structures and creation of R&D "innovation ecosystems", set up of "territorial leaders in R&D00") and PRIN-PNRR INPOWER (P2022PXS5S). H.W., S.M.F., and T.-Q.N. acknowledge the Materials Research Science and Engineering Center (MRSEC) at University of California Santa Barbara (NSF DMR-2308708, IRG-1) for funding. The Material Research Laboratory Shared Experimental Facilities were supported by the MRSEC Program of the National Science Foundation under Award No. DMR 2308708; a member of the NSF-funded Materials Research Facilities Network . The author thank the staff of the ALBA synchrotron, particularly Dr. Eduardo Solano, and Dr. Jaime Martin (Universidade da Coruña) for their assistance with the GIWAXS experiments. A.S. and M.C. acknowledges support by the European Research Council (ERC) under the European Union's Horizon 2020 research and innovation program "ELFO", Grant Agreement 864299. G.C. and M.C. acknowledges support by the European Union's Horizon 2020 research and innovation program under Grant Agreement #964596 "ROBOFOOD". The work of G.M. was financially supported by ICSC-Centro Nazionale di Ricerca in High Performance Computing, Big Data and Quantum Computing, funded by European Union-NextGenerationEU (grant CN00000013) and by the Italian Minister of the University and Research (MUR) within the PRIN-2022 research program (project "NIR+").

Conflict of Interest

The authors declare no conflict of interest.

Data Availability Statement

The data that support the findings of this study are available in the supplementary material of this article.

Keywords

doping, non-covalent interactions, n-type doping, organic semiconductor blends, precursor dopant, thermal activation

Received: March 7, 2025
Revised: April 30, 2025
Published online: June 5, 2025

[1] L. Ding, Z.-D. Yu, X.-Y. Wang, Z.-F. Yao, Y. Lu, C.-Y. Yang, J.-Y. Wang, J. Pei, *Chem. Rev.* **2023**, *123*, 7421.
[2] K. Feng, W. Yang, S. Y. Jeong, S. Ma, Y. Li, J. Wang, Y. Wang, H. Y. Woo, P. K. L. Chan, G. Wang, X. Guo, M. Zhu, *Adv. Mater.* **2023**, *35*, 2210847.
[3] A. Marks, X. Chen, R. Wu, R. B. Rashid, W. Jin, B. D. Paulsen, M. Moser, X. Ji, S. Griggs, D. Meli, X. Wu, H. Bristow, J. Strzalka, N. Gasparini, G. Costantini, S. Fabiano, J. Rivnay, I. McCulloch, *J. Am. Chem. Soc.* **2022**, *144*, 4642.
[4] H.-I. Un, S. A. Gregory, S. K. Mohapatra, M. Xiong, E. Longhi, Y. Lu, S. Rigin, S. Jhulki, C.-Y. Yang, T. V. Timofeeva, J.-Y. Wang, S. K. Yee, S. Barlow, S. R. Marder, J. Pei, *Adv. Energy Mater.* **2019**, *9*, 1900817.
[5] A. S. Sharova, F. Melloni, G. Lanzani, C. J. Bettinger, M. Caironi, *Adv. Mater. Technol.* **2021**, *6*, 2000757.
[6] J. H. Kim, S.-M. Kim, G. Kim, M.-H. Yoon, *Macromol. Biosci.* **2020**, *20*, 2000211.
[7] F. Torricelli, I. Alessandri, E. Macchia, I. Vassalini, M. Maddaloni, L. Torsi, *Adv. Mater. Technol.* **2022**, *7*, 2100445.
[8] J. Y. Gerasimov, A. Halder, A. H. Mousa, S. Ghosh, P. C. Harikesh, T. Abrahamsson, D. Bliman, J. Strandberg, M. Massetti, I. Zozoulenko, D. T. Simon, M. Berggren, R. Olsson, S. Fabiano, *Adv. Funct. Mater.* **2022**, *32*, 2202292.
[9] A. Marrocchi, A. Facchetti, D. Lanari, C. Petrucci, L. Vaccaro, *Energy Environ. Sci.* **2016**, *9*, 763.
[10] J.-X. Chen, Y.-F. Xiao, K. Wang, D. Sun, X.-C. Fan, X. Zhang, M. Zhang, Y.-Z. Shi, J. Yu, F.-X. Geng, C.-S. Lee, X.-H. Zhang, *Angew. Chem., Int. Ed.* **2021**, *60*, 2478.
[11] Y. Lu, J.-Y. Wang, J. Pei, *Acc. Chem. Res.* **2021**, *54*, 2871.
[12] W. Zhao, J. Ding, Y. Zou, C. Di, D. Zhu, *Chem. Soc. Rev.* **2020**, *49*, 7210.
[13] A. D. Scaccabarozzi, A. Basu, F. Aniés, J. Liu, O. Zapata-Arteaga, R. Warren, Y. Firdaus, M. I. Nugraha, Y. Lin, M. Campoy-Quiles, N. Koch, C. Müller, L. Tsetseris, M. Heeney, T. D. Anthopoulos, *Chem. Rev.* **2022**, *122*, 4420.
[14] H. Shi, C. Liu, Q. Jiang, J. Xu, *Adv. Electron. Mater.* **2015**, *1*, 1500017.
[15] L. Bießmann, N. Saxena, N. Hohn, M. A. Hossain, J. G. C. Veinot, P. Müller-Buschbaum, *Adv. Electron. Mater.* **2019**, *5*, 1800654.
[16] M. N. Gueye, A. Carella, N. Massonnet, E. Yvenou, S. Brenet, J. Faure-Vincent, S. Pouget, F. Rieutord, H. Okuno, A. Benayad, R. Demadrille, J.-P. Simonato, *Chem. Mater.* **2016**, *28*, 3462.
[17] A. Schultheiss, A. Carella, S. Pouget, J. Faure-Vincent, R. Demadrille, A. Revaux, J.-P. Simonato, *J. Mater. Chem. C* **2020**, *8*, 17254.
[18] H. Tang, Y. Liang, C. Liu, Z. Hu, Y. Deng, H. Guo, Z. Yu, A. Song, H. Zhao, D. Zhao, Y. Zhang, X. Guo, J. Pei, Y. Ma, Y. Cao, F. Huang, *Nature* **2022**, *611*, 271.
[19] Q. Li, J.-D. Huang, T. Liu, T. P. A. Van Der Pol, Q. Zhang, S. Y. Jeong, M.-A. Stoeckel, H.-Y. Wu, S. Zhang, X. Liu, H. Y. Woo, M. Fahlman, C.-Y. Yang, S. Fabiano, *J. Am. Chem. Soc.* **2024**, *146*, 15860.
[20] S. Griggs, A. Marks, H. Bristow, I. McCulloch, *J. Mater. Chem. C* **2021**, *9*, 8099.
[21] D. Yuan, W. Liu, X. Zhu, *Chem. Soc. Rev.* **2023**, *52*, 3842.
[22] A. G. Werner, F. Li, K. Harada, M. Pfeiffer, T. Fritz, K. Leo, *Appl. Phys. Lett.* **2003**, *82*, 4495.
[23] F. Li, M. Pfeiffer, A. Werner, K. Harada, K. Leo, N. Hayashi, K. Seki, X. Liu, X.-D. Dang, *J. Appl. Phys.* **2006**, *100*, 023716.
[24] S. Guo, S. K. Mohapatra, A. Romanov, T. V. Timofeeva, K. I. Hardcastle, K. Yesudas, C. Risko, J.-L. Brédas, S. R. Marder, S. Barlow, *Chem. – Eur. J.* **2012**, *18*, 14760.
[25] F. Aniés, M. I. Nugraha, A. Fall, J. Panidi, Y. Zhao, P. Vanelle, L. Tsetseris, J. Broggi, T. D. Anthopoulos, M. Heeney, *Adv. Funct. Mater.* **2023**, *33*, 2212305.
[26] P. Wei, J. H. Oh, G. Dong, Z. Bao, *J. Am. Chem. Soc.* **2010**, *132*, 8852.
[27] Y. Zeng, W. Zheng, Y. Guo, G. Han, Y. Yi, *J. Mater. Chem. A* **2020**, *8*, 8323.
[28] B. Saglio, M. Mura, M. Massetti, F. Scuratti, D. Beretta, X. Jiao, C. R. McNeill, M. Sommer, A. Famulari, G. Lanzani, M. Caironi, C. Bertarelli, *J. Mater. Chem. A* **2018**, *6*, 15294.
[29] B. D. Naab, S. Zhang, K. Vandewal, A. Salleo, S. Barlow, S. R. Marder, Z. Bao, *Adv. Mater.* **2014**, *26*, 4268.
[30] O. Bardagot, C. Aumaître, A. Monmagnon, J. Pécaut, P.-A. Bayle, R. Demadrille, *Appl. Phys. Lett.* **2021**, *118*, 203904.
[31] S. Jhulki, H.-I. Un, Y.-F. Ding, C. Risko, S. K. Mohapatra, J. Pei, S. Barlow, S. R. Marder, *Chem* **2021**, *7*, 1050.
[32] B. D. Naab, S. Guo, S. Olthof, E. G. B. Evans, P. Wei, G. L. Millhauser, A. Kahn, S. Barlow, S. R. Marder, Z. Bao, *J. Am. Chem. Soc.* **2013**, *135*, 15018.
[33] F. Pallini, S. Mattiello, N. Manfredi, S. Mecca, A. Fedorov, M. Sassi, K. Al Kurdi, Y.-F. Ding, C.-K. Pan, J. Pei, S. Barlow, S. R. Marder, T.-Q. Nguyen, L. Beverina, *J. Mater. Chem. A* **2023**, *11*, 8192.
[34] S. Cimò, I. Denti, L. Rossi, M. Cassinelli, M. Rossi, R. Castagna, G. LeCroy, A. Salleo, M. Caironi, A. Famulari, C. Castiglioni, C. Bertarelli, *Adv. Sci.* **2025**, *12*, 2402482.
[35] O. Bardagot, Y. Kervella, A. A. Medjahed, S. Pouget, T. N. Domschke, A. Carella, C. Aumaître, P. Lévêque, R. Demadrille, *J. Mater. Chem. C* **2023**, *11*, 14108.
[36] R. A. Schlitz, F. G. Brunetti, A. M. Glaudell, P. L. Miller, M. A. Brady, C. J. Takacs, C. J. Hawker, M. L. Chabinyc, *Adv. Mater.* **2014**, *26*, 2825.
[37] P. Rossi, F. Pallini, G. Coco, S. Mattiello, W. L. Tan, L. Mezzomo, M. Cassinelli, G. Lanzani, C. R. McNeill, L. Beverina, M. Caironi, *Adv. Mater. Interfaces* **2023**, *10*, 2202416.
[38] F. Pallini, S. Mattiello, M. Cassinelli, P. Rossi, S. Mecca, W. L. Tan, M. Sassi, G. Lanzani, C. R. McNeill, M. Caironi, L. Beverina, *ACS Appl. Energy Mater.* **2022**, *5*, 2421.
[39] C. Li, W. Wang, C. Zhan, Q. Zhou, D. Dong, S. Xiao, *J. Mater. Chem. C* **2023**, *11*, 15599.
[40] L. Qiu, J. Liu, R. Alessandri, X. Qiu, M. Koopmans, R. W. A. Havenith, S. J. Marrink, R. C. Chiechi, L. J. Anton Koster, J. C. Hummelen, *J. Mater. Chem. A* **2017**, *5*, 21234.
[41] J. Han, A. Chiu, C. Ganley, P. McGuiggan, S. M. Thon, P. Clancy, H. E. Katz, *Angew. Chem., Int. Ed.* **2021**, *60*, 27212.
[42] S. Wang, T.-P. Ruoko, G. Wang, S. Riera-Galindo, S. Hultmark, Y. Puttisong, F. Moro, H. Yan, W. M. Chen, M. Berggren, C. Müller, S. Fabiano, *ACS Appl. Mater. Interfaces* **2020**, *12*, 53003.
[43] F. Pallini, G. Garavaglia, G. Paoli, G. Mattioli, F. Porcelli, L. Mezzomo, D. Florenzano, R. Ruffo, M. Sassi, S. Mattiello, *ChemRxiv* **2025**.
[44] C. Xu, D. Wang, *J. Mater. Chem. A* **2023**, *11*, 15416.
[45] S. Riera-Galindo, A. Orbelli Biroli, A. Forni, Y. Puttisong, F. Tessore, M. Pizzotti, E. Pavlopoulou, E. Solano, S. Wang, G. Wang, T.-P. Ruoko, W. M. Chen, M. Kemerink, M. Berggren, G. di Carlo, S. Fabiano, *ACS Appl. Mater. Interfaces* **2019**, *11*, 37981.
[46] C. Dardonville, M. L. Jimeno, I. Alkorta, J. Elguero, *Org. Biomol. Chem.* **2004**, *2*, 1587.
[47] R. Steyrleuthner, M. Schubert, I. Howard, B. Klaumünzer, K. Schilling, Z. Chen, P. Saalfrank, F. Laquai, A. Facchetti, D. Neher, *J. Am. Chem. Soc.* **2012**, *134*, 18303.
[48] M. Caironi, M. Bird, D. Fazzi, Z. Chen, R. Di Pietro, C. Newman, A. Facchetti, H. Sirringhaus, *Adv. Funct. Mater.* **2011**, *21*, 3371.
[49] D. Trefz, A. Ruff, R. Tkachov, M. Wieland, M. Goll, A. Kiriy, S. Ludwigs, *J. Phys. Chem. C* **2015**, *119*, 22760.
[50] R. Steyrleuthner, R. Di Pietro, B. A. Collins, F. Polzer, S. Himmelberger, M. Schubert, Z. Chen, S. Zhang, A. Salleo, H. Ade, A. Facchetti, D. Neher, *J. Am. Chem. Soc.* **2014**, *136*, 4245.
[51] J. Rivnay, R. Steyrleuthner, L. H. Jimison, A. Casadei, Z. Chen, M. F. Toney, A. Facchetti, D. Neher, A. Salleo, *Macromolecules* **2011**, *44*, 5246.
[52] J. Rivnay, M. F. Toney, Y. Zheng, I. V. Kauvar, Z. Chen, V. Wagner, A. Facchetti, A. Salleo, *Adv. Mater.* **2010**, *22*, 4359.

[53] A. Luzio, L. Criante, V. D'Innocenzo, M. Caironi, *Sci. Rep.* **2013**, *3*, 3425.
[54] H. Guo, C.-Y. Yang, X. Zhang, A. Motta, K. Feng, Y. Xia, Y. Shi, Z. Wu, K. Yang, J. Chen, Q. Liao, Y. Tang, H. Sun, H. Y. Woo, S. Fabiano, A. Facchetti, X. Guo, *Nature* **2021**, *599*, 67.
[55] F. Pallini, PhD dissertation, Milano-Bicocca, Milano **2024**.
[56] R. Matsidik, H. Komber, A. Luzio, M. Caironi, M. Sommer, *J. Am. Chem. Soc.* **2015**, *137*, 6705.
[57] S. S. Zalesskiy, V. P. Ananikov, *Organometallics* **2012**, *31*, 2302.
[58] A. Nogales, E. Gutiérrez, 2D Representation of a Wide Angle X Ray Scattering Pattern as a Function of Q Vector Components **2019**, MathWorks File Exchange.
[59] P. Pracht, F. Bohle, S. Grimme, *Phys. Chem. Chem. Phys.* **2020**, *22*, 7169.
[60] C. Bannwarth, S. Ehlert, S. Grimme, *J. Chem. Theory Comput.* **2019**, *15*, 1652.
[61] F. Neese, *WIREs Comput. Mol. Sci.* **2012**, *2*, 73.
[62] F. Weigend, R. Ahlrichs, *Phys. Chem. Chem. Phys.* **2005**, *7*, 3297.
[63] A. Schäfer, H. Horn, R. Ahlrichs, *J. Chem. Phys.* **1992**, *97*, 2571.
[64] A. D. Becke, *J. Chem. Phys.* **1993**, *98*, 5648.
[65] S. Grimme, J. Antony, S. Ehrlich, H. Krieg, *J. Chem. Phys.* **2010**, *132*, 154104.
[66] Y. Zhao, D. G. Truhlar, *Theor. Chem. Acc.* **2008**, *120*, 215.
[67] V. Barone, M. Cossi, *J. Phys. Chem. A* **1998**, *102*, 1995.
[68] S. Spicher, S. Grimme, *Angew. Chem., Int. Ed.* **2020**, *59*, 15665.
[69] L. Martínez, R. Andrade, E. G. Birgin, J. M. Martínez, *J. Comput. Chem.* **2009**, *30*, 2157.